# Transient volume stabilization reveals the key role a PM permeability in pyroptotic cell swelling

**Estelle Bastien[a,b,2], Guillaume Duprez[a], Hélène Delanoë-Ayari[a], Charlotte Rivière[a], Virginie Petrilli[c], Pierre Recho[b,1,2], and Sylvain Monnier[a,1,2]**

This manuscript was compiled on March 27, 2025

**Pyroptosis, an inflammatory form of cell death, is associated with large cell swelling and plasma membrane rupture. Recently, such swelling has been shown to occur in a two steps fashion, but the precise molecular and biophysic mechanisms driving the process remain elusive. We demonstrate through advanced quantitative microscopy that, between the two swelling phases, cell volume stabilizes, while plasma membrane permeability to ions and small molecules is markedly elevated due to the formation of pores. From a biophysical perspective, how such a volume plateau exists is puzzling as ion pumps should not regulate the cell volume in these conditions. To address this, we developed a physical model based on an ions pump-and-leak framework, incorporating the dynamics of non-selective pore formation. We experimentally identify two distinct pore permeability dynamics, associated to an increase in the water filtration coefficient and to an ion selectivity decrease due to pore opening. Altogether our results suggest the existence of two mechanistically different pore types, likely driven by separate molecular players. Our findings provide fundamental insights into the biophysics of cell death and may have broader implications for understanding membrane rupture in other pathological contexts.**

cell volume | cell mechanics | cell death | pyroptosis

## Significance Statement

Among various programmed lytic cell death, pyroptosis is marked by dramatic changes in cell shape and large fluctuations in volume, fundamentally altering the cell's physical properties. These biophysical changes are not mere byproducts but integral components of the death process, closely interacting with molecular events. By combining optogenetics, quantitative microscopy, and modeling, we show that a progressive increase in plasma membrane permeability alone drives cell swelling and membrane lysis. We therefore demonstrate that a deeper understanding of these dynamic cell modifications and their consequences will shed light on the molecular and biophysical mechanisms driving different forms of cell death.

Cell death, a fundamental biological process, is often accompanied by profound morphological changes. Notably, Pyroptosis - a key pro-inflammatory form of cell death - is characterized by a drastic cell volume dysregulation with distinct morphological events, including membrane blebbing, cell swelling, and plasma membrane (PM) rupture, ultimately resulting in the release of intracellular content that enhances inflammation (1). Pyroptosis is triggered by pathogens that activate innate immune receptors, leading to the assembly of large macromolecular complexes known as inflammasomes (2). The adaptor ASC (ASC) within these complexes recruits and activates the cysteine protease caspase-1 (CASP1) to form micrometer-scale aggregates called specks, a hallmark of inflammasome activation. Inflammasome signaling leads to the CASP1-dependent cleavage of proinflammatory cytokines, such as pro-interleukin 1$\beta$ (pro–IL-1$\beta$), and gasdermin D (GSDMD). The cleaved GSDMD N-terminal domains oligomerize and form pores in the PM significantly impacting its permeability (3–5).

Formation of pores in the PM is an essential feature of the pyroptotic cell death program (6). GSDMD pore formation is a dynamic process involving the oligomerization and membrane insertion of the N-terminal fragment of GSDMD after its cleavage by CASP1 (3, 5). Previous studies suggest that GSDMD pores exist in various shapes, including rings, arcs, and slits, which can grow, fuse and mature (7, 8), reaching an internal radius of approximately 10.5 nm within minutes after their initiation (9). Furthermore, these pores were demonstrated to dynamically open and close, allowing the pyroptosis process to be reversible (10). However, these findings are based on *in vitro* and *in silico* models, and the precise assembly process and the opening dynamic of GSDMD pores in live cells remain unknown.

GSDMD pores are known to be non-selective with respect to small solutes, allowing the diffusion across the PM of water, ions (11), as well as fluorescent dyes and small proteins like interleukin IL-1$\beta$ (12–14), which has a hydrodynamic radius ($R_H$) of 2.25 nm (15). In contrast, larger molecules, such as LDH ($R_H = 4.8$ nm) (1) and high-molecular-weight dextran cannot cross the PM (1, 13, 16). Such exclusion of LDH shows that the radius of GSDMD pores measured from electron microscopy does not fully determine the transport through GSDMD pore. This discrepancy suggest a certain level of

Author affiliations: [a]University of Lyon, Université Claude Bernard Lyon 1, CNRS, Institut Lumière Matière, F-69622, VILLEURBANNE, France.; [b]Université Grenoble Alpes, CNRS, LIPHY, 38000 Grenoble, France; [c]CRCL, Centre de Recherche en Cancérologie de Lyon, INSERM U1052, CNRS UMR5286, Université de Lyon, Université Lyon 1; Centre Léon Bérard F-69000 Lyon, France

Please provide details of author contributions here.

Please declare any competing interests here.

[1]P.R. contributed equally to this work with S.M.

[2]To whom correspondence should be addressed. E-mail: estelle.bastienuniv-lyon1.fr, pierre.rechouniv-grenoble-alpes.fr and sylvain.monnieruniv-lyon1.fr

DRAFT

control of GSDMD pores on the transport of internal cargo, which could have various physical origins such as a partial opening of the pores (17), or electro-chemical gating (18). Large molecules released during pyroptosis can still cross the PM thanks to the formation of lesions generated by the PM resident protein ninjurin-1 (Ninj1) (16, 19). While these studies show that PM permeability is a key feature of pyroptosis, its biophysical mechanisms remain largely unexplored (20).

The transport across mammalian cell membranes is generally considered to be selective, meaning that ions and water move through the PM via independent routes: ions channels (passive) and ion pumps (active) for ions and aquaporins for water. The integration of such selectivity principle in phenomenological models of water and ions fluxes has been formalized in the Kedem-Katchalsky close-to-equilibrium thermodynamic framework (21, 22) and the relation

$$J_w \propto \Delta p - \Delta\Pi, \qquad [1]$$

between $J_w$ the water flux and $\Delta p$ and $\Delta\Pi$, the hydrostatic and osmotic pressures difference across the PM is very widely used in cell volume regulation models (23–27).

Relying on relation Eq. (1), the textbook paradigm that allows to understand how a mammalian cell controls its volume is the so called pump-and-leak model (23, 28). The model allows to maintain the same osmolarity between the cell cytoplasm and the extra-cellular medium by effectively pumping ions out of the cell at a certain rate to counter the passive osmotic effect that tends to homogenize concentrations. Therefore the fact that the cell volume does not swell to infinity in normal situations is related to a non-dimensional parameter comparing the kinetics of active pumping to that of passive leaking.

A correction can be brought by the cell surface and bulk cytoskeleton (29) which also provide an elastic resistance to infinite swelling. However, the typical measured stiffnesses of the cytoskeleton ($\sim 0.1 - 1$ kPa) are in general negligible compared to that induced by a 10 mM variation of osmotic pressure ($\sim 25$ kPa), which is a fluctuation expected to occur in extracellular media that are typically of few hundreds of milimolar. Upon, permeabilization of the PM, one may therefore expect that the passive leaking will completely dominate the active pumping and lead to a very large cell swelling. Since the excess PM surface area stored in membrane invaginations is limited (26, 30), it was widely assumed that the ensuing mechanical stress alone would inevitably rupture the PM - until the discovery of Ninj1 changed this paradigm (16, 31).

Indeed, the historical model suggests that GSDMD pores trigger rapid ion fluxes, osmotic swelling, and mechanical stress that culminate in cell lysis (1, 6). However, it has recently been shown that Ninj1 is necessary for the formation of PM lesions and the release of large molecules (16). A recent biophysical study revealed a two-step cell swelling process not limited by the amount of PM, confirming that the lysis process is not purely mechanical as it was thought earlier (31). The mechanisms of Ninj1 action, the link between GSDMD pore opening and Ninj1 lesion occurrence, and, more broadly, the processes linking cell swelling to PM rupture remain open questions currently under intensive investigations (32).

In this study, we combined an optogenetic approach with single-cell volume probing to dissect the dynamics of cell swelling, focusing specifically on pore formation and PM permeability (31). To achieve a comprehensive understanding of these processes, we developed a theoretical framework to model cell volume and PM permeability changes during pyroptosis. Despite the expected full permeabilization of the PM to ions by GSDMD pores, cell volume stabilizes at approximately 1.4 times its initial size. This transient phase persists for a few minutes, during which we observe a gradual enlargement of pores before a secondary swelling phase starts that culminates with the PM rupture. By developing a simple model to explain the non trivial volume dynamics, we emphasize the need to carefully reconsider the commonly assumed selectivity constraints in Eq. (1) when modeling cell volume regulation.

## Results

**Dynamic Correlation of Swelling and PM Permeabilization.** We leveraged an optogenetic approach — previously developed in our lab — to directly activate the inflammasome pathway while bypassing the non-specific and uncontrolled upstream signaling perturbating cell volume (31) (Fig. 1 A). Using this approach, we reconstructed the volume dynamics (35, 36), leading to pyroptotic cell lysis at the single-cell level with high temporal resolution ($< 10s$) (Figs.1 B and 2 A-D). Briefly, as long as the PM prevents a dye from entering the cell, volume is estimated by integrating the fluorescence signal of this dye over the cell area (31). Once the dye crosses the PM, fluorescence intensity increases, corresponding to a drop in the measured volume and indicating PM permeabilization to a dye of known size (Fig.2 B&D) indicating the presence of PM pores at least as large as the dye. By using a broad range of probes with varying hydrodynamic radii, the occurrence of PM pores of different sizes is monitored (Fig.1D). This study was conducted on immortalized bone marrow-derived macrophages (iBMDMs), a well-established model in which pyroptosis naturally occurs as part of the immune response. To validate our findings, all experiments were also performed on a second cell line, mouse embryonic fibroblasts (MEFs).

Two distinct swelling phases can be distinguished, separated by a volume plateau. This plateau ends with the entry of a 10 kDa dextran dye (See 10 kDa in Fig.2 B, Fig. S2 B), which corresponds to the onset of a second swelling phase (See 500 kDa in Fig.2 B, Fig. S2 B). Maximum swelling is reached when a 500 kDa dextran dye enters the cell that we identified as the PM lysis with lesions larger than the GSDMD pores ($R_H^{500} > R_{GDSMD}$ that may be attribute to Ninj1 (16, 31). These two swelling phases correspond to distinct morphological changes (Fig. S1): the initial volume increase is associated with multiple blebs, whereas the second phase is characterized by one or two large blebs that continue expanding until PM rupture.

Co-incubation with 10 kDa dextran ($R_H = 1.9$ nm) and SRB a small soluble fluorophore ($R_H = 0.5$ nm), for which the PM is initially impermeable, revealed a strong correlation ($p < 0.001$) between the onset of swelling and SRB entry in the cell (Fig. 2 C&D&E and Fig. S2 A). These data indicate that PM integrity is compromised early during pyroptosis, allowing the influx of water and ions and suggesting that an increase in PM permeability drives the first swelling phase.

DRAFT

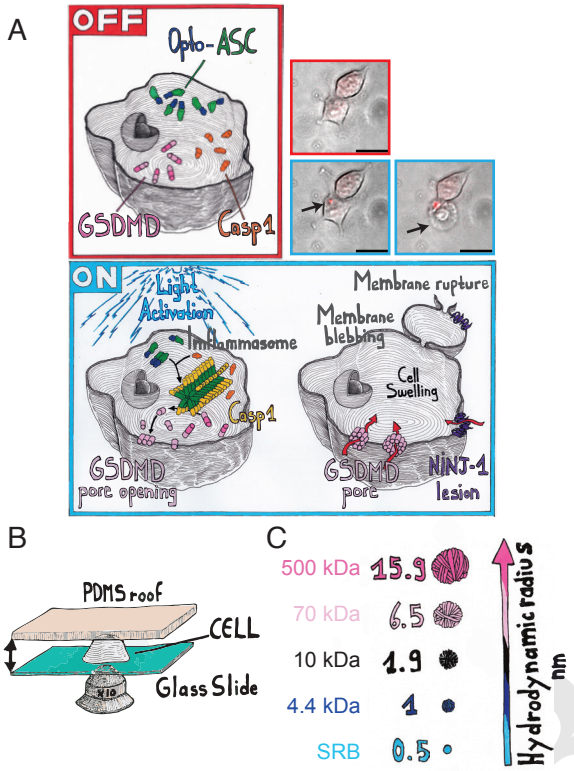


**Fig. 1. Optogenetic control of pyroptosis in a cell model combined with advanced time-resolved microscopy.** (A) Schematic representation of the optogenetic cell model used to control pyroptosis induction. In the OFF state, cells expressing GSDMD and CASP-1, key players of pyroptosis, grow normally. These cells stably express an optogenetic construct, opto-ASC, which consists of a chimeric fusion of the fluorescent protein RFP (for tracking), a photoactivable CRY2 domain, and ASC. Upon blue light activation (ON state), CRY2 induces ASC oligomerization, recruiting CASP-1 to activate the inflammasome and speck formation. This leads to GSDMD cleavage and pore formation via the insertion and oligomerization of the GSDMD N-terminal fragment in the PM. Rapid ions and water influx trigger cell swelling, PM blebbing, and PM rupture (PMR) via Ninj1 (31). Merge brightfield and fluorescence images of optogenetically modified iBMDM cells undergoing pyroptosis upon light activation. In the ON state, speck formation (red spot, RFP signal), a hallmark of inflammasome activation, is followed by PM blebbing (white arrow). (B) Single-cell analysis using fluorescence exclusion microscopy (FXM). Cells were seeded in a PDMS microfabricated chamber of known height and incubated with medium containing fluorescent dyes or dextrans conjugated to fluorescent probes of varying hydrodynamic radii (0.5 $nm$ for SRB to 15.9 $nm$ for 500 kDa dextran, C, Sources from (33, 34)). Upon blue light activation, time-dependent changes in cell volume were monitored, and PM permeability as well as pore size dynamics were assessed based on the entry of fluorescent probes of different sizes.

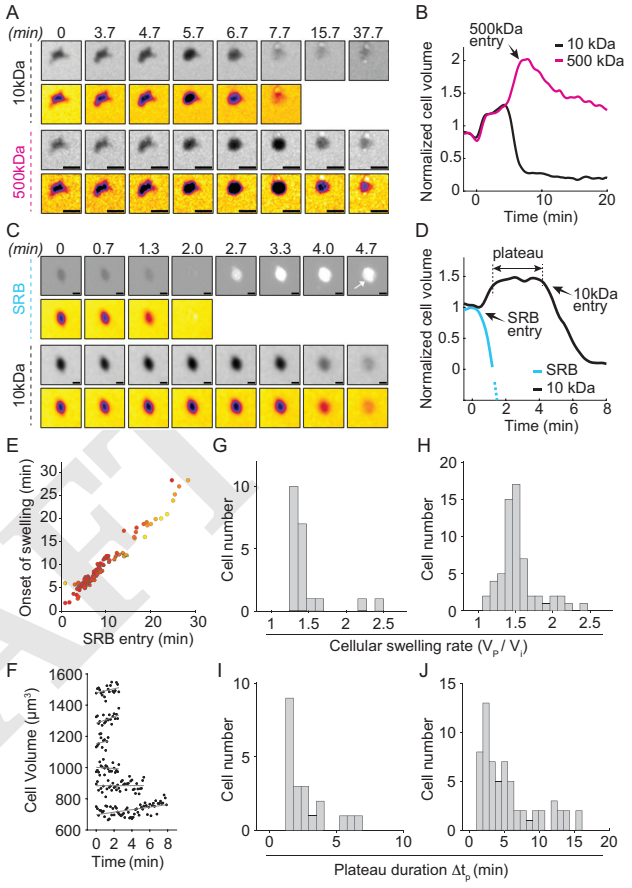


**Fig. 2. The swelling of the pyroptotic cell reveals a phase of volume steady state.** (A,C) FXM timelapse images of iBMDM cells undergoing pyroptosis with different sets of fluorescent probes: (A) 10 kDa Dextran-A647 and 500 kDa Dextran-TRITC; (C) Sulforhodamine B (SRB) and 10 kDa Dextran-A647 (Scale bar 20 $\mu m$). Corresponding normalized single-cell volume trajectories (relative to the initial volume $V_i$ before swelling at $t_0$) are shown in (B) and (D), respectively. The black arrows indicate the entry of dyes into the cell, determined by a drop in cell volume. The dotted line marks the plateau of cell volume, determined from 10 kDa Dextran-A647 volume trajectories, indicating a volume steady state. (E) Correlation between the timing of SRB entry into the cell and the onset of cell swelling (pearson correlation $p < 0.001$), with a color gradient from red to green to yellow representing the degree of correlation. (F) Examples of volume steady-states, determined as a volume plateau ($V_p$) observed for several iBMDM cells. Characterization of the volume steady-state with distributions of the cellular swelling rates required to reach this state ($V_p/V_i$) and its duration ($\Delta t_p$), for iBMDM (G - I) and MEFs (H - J). for (A, B) N=1, n= 31 cells, for (C, D, E) N=3, n= 101 cells, for (G, H) N= 3, n= 21 cells and for (I, J) N= 3, n= 79 cells.

DRAFT

In addition, GSDMD deletion abolished cell swelling and inhibition of Na/H pumps involved in volume regulation had no significant effect on swelling (Fig. S2 D-F). Together, these results indicate that GSDMD pores are essential for PM permeabilization, driving the initial swelling phase, consistent with previous reports that GSDMD is required for pyroptosis-induced swelling (6). At this stage, the PM remains impermeable to molecules larger than $R_H^{10} = 1.9$ nm, as 10 kDa dextran does not enter the cell.

**A volume steady-state with permeable PM.** During pyroptosis-induced PM permeabilization, all cells from iBMDM and MEF cell lines exhibit a shoulder during swelling of variable durations (from 30 seconds to 15 minutes; Fig.2 F and Fig. S2 G). For quantification, we defined as a plateau situations when the cell volume is nearly constant ($\Delta V/V_p <$ 10%) for at least 1 minute. Such a volume plateau was observed in both cell lines, with 26 % of iBMDMs and 40 % of MEFs displaying a plateau. The plateau duration was $\Delta t_p = 2.59 \pm 1.70$ min for iBMDMs and $\Delta t_p = 5.56 \pm 4.05$min for MEFs (Fig.2 G& I). The relative volume at the plateau, $V_p/V_i$ is $1.5 \pm 0.3$ for both iBMDMs and MEFs (Fig.2 H&J).

The existence of this volume stabilization, despite the PM being permeable to water and ions is unexpected. Indeed, one would anticipate that a cell with a compromised PM would continue to swell indefinitely as ion pumps become unable to counteract the passive osmotic swelling.

**Gradual pore opening.** Pyroptosis-induced PM permeabilization is a dynamic process involving at least a combination of GSDMD and Ninj-1 proteins. For the first time, by tracking the sequential entry of fluorescent dyes with defined hydrodynamic radii into the cell, we are able to assess this dynamic process in real time. This approach enables us to estimate the evolution of pore radii at the PM (Fig.1C, Fig.3 A-D). SRB entry marks the first detectable event of PM permeabilization and coincides with the onset of cell swelling (Fig. 2 D). It therefore sets the starting time of pyroptotic swelling and was used as a reference for the entry times of other probes (Fig. 3 E& F).

Our measurements then revealed a sequential entry of fluorescent probes according to their hydrodynamic radius (Fig. 3 E&F). We computed the kinetics of PM pore enlargement by fitting the timing of probe entry with their hydrodynamic radius. Two distinct behaviors were observed; 1 - The entry of SRB and small dextrans (4.4 and 10 kDa) allowed us to estimate a pore opening speed of 0.29 nm/min (Fig. 3 E). 2 - The entry of 70 kDa and 500 kDa dextrans displayed a faster opening speed of 1.84 nm/min (Fig. 3 F). This different dynamics in PM permeability suggests that the two swelling phases arise from two different actors. Natural candidates would be GSDMD which facilitates the initial entry of small dyes, and Ninj1, which acts at a later stage to create large lesions, enabling the passage of large proteins such as LDH ($R_H^{LDH} = 4.8$ nm).

Our results reveal two distinct swelling phases driven by increased PM permeability, due to pore enlargement probably accompanied by a rise in total pore surface. The phases are separated by a volume stabilization that cannot be explained by classical models of cell volume control. Such observations highlight the need for a tailored theoretical model to describe cell volume dynamics and membrane fluxes

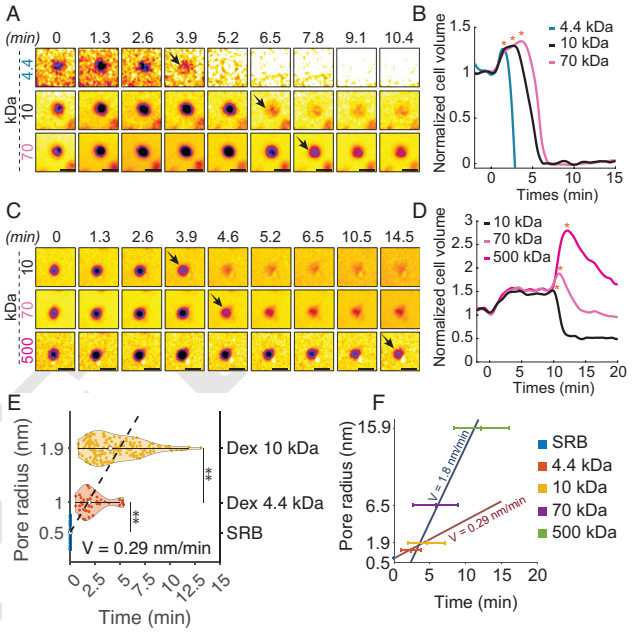


**Fig. 3. Linear relationship between fluorescent probe hydrodynamic radius and entry: Progressive opening of GSDMD pores and Ninj1 lesion size.** (A, C) FXM timelapse images of iBMDM cells undergoing pyroptosis while co-incubated with different sets of fluorescent dextrans: (A) 4.4 kDa Dextran-TRITC, 10 kDa Dextran-A647, and 70 kDa Dextran-FITC; (C) 10 kDa Dextran-A647, 70 kDa Dextran-FITC, and 500 kDa Dextran-TRITC (Scale bar 20 $\mu$m, arrow indicates probe cell entry). Corresponding normalized single-cell volume trajectories (relative to the initial volume at T0, before swelling) are shown in (B) and (D), respectively. (E) The kinetics of minimal GSDMD pore opening and the speed of pore expansion were determined as a function of probe entry timing ($R_H$ ranging from 0.5 to 1.9 nm).The violin plot represents the distribution of data points (colored dots), with the median indicated by the white dot. Similarly, using the full range of $R_H$ probe entry times, the kinetics of minimal GSDMD pore and Ninj1 lesion opening were assessed, with the data presented as mean $\pm$ standard deviation (F). Probe entry times were determined from the trajectories of individual cell volumes and correspond to the time interval between the onset of cell swelling ($T_0$) and the volume signal drop for each probe (orange star). for (A,B,E) N=3, n= 49 cells, and for (C,D,F (70kDa and 500 kDA dextran data)) N=1, n= 31 cells. Paired-sample t-test, $^{**}$ $p < 0.05$;

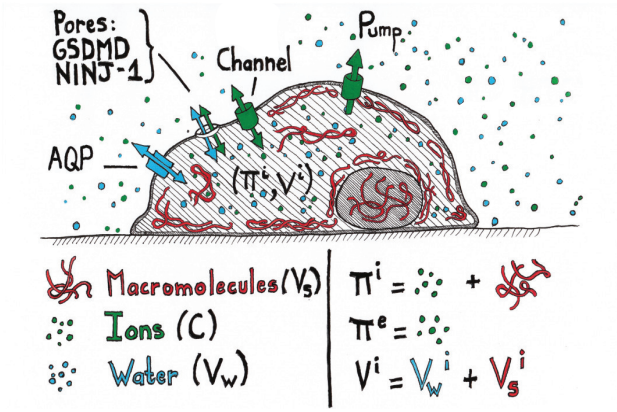


**Fig. 4.** Schematic of the cell volume model. The internal osmotic pressure is caused by the entropy of mixing between macromolecules and ions with water. The external osmotic pressure is only caused by ions. The exchanges at the PM can follow several routes. Ions can travel through channels and pumps while water travels through aquaporins. GSDMS pores are permeable to both water and ions.

at the PM, providing deeper insight into the physics of pyroptotic swelling.

**Model for the cell volume control.** Before the formation of GSDMD pores, the PM is a highly selective interface (21) and we propose the following simple model for cell volume regulation, only valid at a timescale where synthesis does not increase the cell dry mass in a significant way. Eq. (2) describe the temporal evolution of the volume of water and ion mass within the cell. See (37) for a detailed thermodynamic close-to-equilibrium derivation of Eq. (2). A scheme of the model is shown on Fig. 4:

$$\begin{aligned} \frac{dV_w^i}{dt} &= L_p\left(RTC^i + \frac{\rho_s RT\nu}{M_s}\phi_s + \frac{\rho RT}{2M_w}\phi_s^2 - RTC^e\right) \\ M\frac{d(C^iV_w^i)}{dt} &= P\frac{RT}{M}\ln\left(\frac{C^e}{C^i}\right) - p \end{aligned} \quad [2]$$

In Eq. (2), $V_w^i$ represents the volume of water contained in the cell and $C^i$ is the molar ions concentration in the cell cytoplasm. Water is driven through the PM by the difference of osmotic pressures on both sides with a filtration coefficient $L_p$. The external osmotic pressure $RTC^e$ is, in a dilute approximation, only due to the entropy of mixing of the external ions of concentration $C^e$ where $R$ is the gas constant and $T$ the temperature. Retaining again only generic entropic terms, the internal osmotic pressure contains three terms. The ions in solution in the solvent lead to the term $RTC^i$, their molar mass is denoted by $M$. . The configurational interaction between the water and large macromolecules (38) leads to the two other terms that depend on the cell dry mass volume fraction:

$$\phi_s = \frac{V_s^i}{V^i} \text{ with } V^i = V_s^i + V_w^i,$$

where $V_s^i$ is the fixed volume occupied by the macromolecules and $V^i$ is the total cell volume (the volume occupied by ions is neglected). The $\phi_s$ term in Eq. (2) is proportional to the molar concentration of macromolecules in the cytoplasm but, in the Flory-Huggins entropy of mixing there is also a $-\phi_s - \ln(1-\phi_s) \sim \phi_s^2/2$ term which is quantitatively important. See (37) for details.

| name & symbol & typical value | | |
|---|---|---|
| PM permeability | $P$ | $5\times10^{-15}$g/m$^2$s(23) |
| ion export rate | $p$ | $1.4\times10^{-14}$ g/s (27, 39–41) |
| ion molar mass | $M$ | 22 g/mol |
| metabolites molar mass | $M_s$ | 200 g/mol |
| PM filtration | $L_p$ | $5\times10^{-22}$m$^3$/s/Pa (28, 42) |
| proportion of metabolites | $\nu$ | 17% (27) |
| external ion concentration | $C^e$ | 300 mM (28) |
| mass density of metabolites | $\rho_s$ | 1300 g/L |
| mass density of water | $\rho_w$ | 1000 g/L |
| cell radius | $R^i$ | 10$\mu$m |
| Volume of dry mass | $V_s^i$ | $2\times10^{-16}$m$^3$ (35) |
| characteristic time | $\tau = V_s^i/(L_pRTC^e)$ | 0.6 s |
| water mixing | $A = \rho_w/(2M_wC^e)$ | 93 |
| metabolites mixing | $B = \rho_s\nu/(M_sC^e)$ | 3.7 |
| pump to leak ratio | $\alpha = pM/(PRT)$ | 1.96 |
| ions vs water transport | $\epsilon = P/(L_p(C^eM)^2)$ | $3\times10^{-4}$ |
| filtration timescale | $\tau = V_s^i/(L_pRTC^e)$ | 0.6 s |

**Table 1. Rough estimates of the model** Eq. (2) **parameters. Details about how to obtain these effective parameters are given in (37).**

The mass density and the molar mass of water (resp. macromolecules) are denoted $\rho$ and $M_w$ (resp. $\rho_s$ and $M_s$). The parameter $\nu \simeq 0.17$ (27) represents the fraction of metabolites among macromolecules since proteins and chromatin contributions are negligible due to their high molar masses (see (37) for details). The mechanical contribution of the PM/cortex complex ($\Delta p$ term in Eq. (1)) is neglected in Eq. (2) compared to the osmotic contribution. See (37) for a quantitative justification. The ions move across the PM via selective channels with a permeability $P$ and are pumped out at an effective rate $p$.

Introducing the non-dimensional parameters $A$, $B$, $\alpha$ and $\epsilon$ and the PM water filtration timescale $\tau$ defined in Table 1, we can rewrite Eq. (2)

$$\begin{aligned} \tau\frac{d(\phi_s^{-1}-1)}{d\hat{t}} &= A\phi_s^2 + B\phi_s + \chi - 1 \\ \tau\frac{d\chi(\phi_s^{-1}-1)}{d\hat{t}} &= -\epsilon(\ln(\chi)+\alpha), \end{aligned} \quad [3]$$

where $\chi = C^i/C^e$ represents the internal ions concentration in the cell compared to the concentration imposed outside. The parameter $A$ and $B$ represent the osmotic pressure of the mixing of water and macromolecules compared to the external osmotic pressure of the ions. $\alpha$ is the pump to leak ratio: the ratio between the rate of active ions pumping compared to the rate of their passive osmotic leaking. Finally $\epsilon$ controls the permeability of the PM to ions compared to that of water.

This very simple physical model neglects electrostatic effects (27), the differential PM permeabilities of various ions species and the stoichiometry of the pumping mechanisms (23, 43, 44), the various mechanotransduction pathways that affect the PM permeability (24–26) as well as the biochemical regulation of the ion channels and pumps (45). Nevertheless, based on rough experimental data collected in Table 1, the steady state dry mass volume fraction $\bar{\phi}_s$ of Eq. (3),

$$\bar{\phi}_s = \frac{\sqrt{4A\left(1-e^{-\alpha}\right)+B^2} - B}{2A} \text{ and } \bar{\chi} = e^{-\alpha} \quad [4]$$

provides the value $\bar{\phi}_s \approx 0.08$. This is close to the value experimentally found for HeLa cells in (35) for which the mean

DRAFT

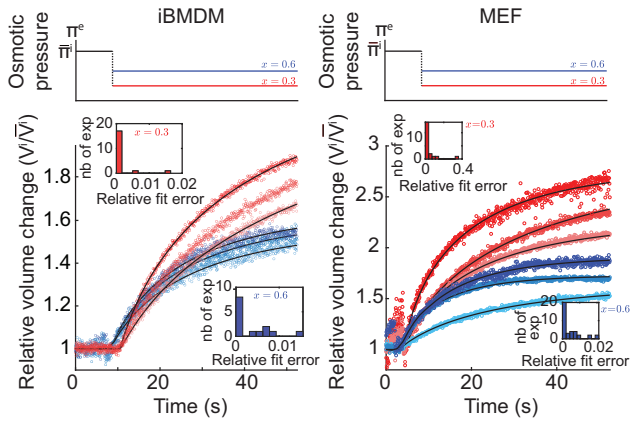


**Fig. 5. Modelling osmotic perturbations.** Top, dynamics of osmotic pressure application. Bottom, examples of the experimental volume dynamics and fits according to the model Eq. (5) for (A) iBMDM and (B) MEF cells. The red curves correspond to a $x = 0.3$ dilution factor and the blue $x = 0.6$. The inset plots are bins of the relative squared error between the data and the fit for all the performed experiments in each hypoosmotic condition (For iBMDM cells, $n = 14$ for $x = 0.6$ and $n = 19$ for $x = 0.3$. For MEFs, $n = 37$ for $x = 0.6$ and $n = 10$ for $x = 0.3$). See Material & methods for the fitting parameters

volume during the cell cycle is $V^i \approx 2700\mu\text{m}^3$ and the mean dry mass is $\rho_s V_s^i \approx 255$pg. Taking for $\rho_s \approx 1300$ g/L (based on the rough estimates of the mass densities of chromatin 1700 g/L, lipids 950 g/L, proteins 1300 g/L and sugars 1500 g/L), the approximate mass fraction of macromolecules, is $\bar{\phi}_s \approx 0.07$.

To test the model more quantitatively, we perform hypo-osmotic shocks on iBMDM cells by dilution of the external medium and measure their volume with FXm (Fig. 5). This dilution leads to a change of $C^e$ to $xC^e$ where $x < 1$ is the dilution factor. Owing to the fact that ion transport is slow compared to that of water ($\epsilon \ll 1$, see Table 1), we can assume that the number of ions does not change ($d(C^i V_w^i)/dt \approx 0$) in Eq. (3) leading to the approximation $C^i V_w^i = \bar{C}^i \bar{V}_w^i$ in the tens of seconds following the shock. The bar quantities denote the isotonic situation before the shock.

The cell volume dynamic during the shock is therefore given by the first relation in Eq. (3):

$$\tau \frac{d\phi_s}{dt} = \phi_s^2 \left( x_t - \frac{\bar{\phi}_s^{-1} - 1}{\phi_s^{-1} - 1} \mathrm{e}^{-\alpha} - B\phi_s - A\phi_s^2 \right). \qquad [5]$$

In Eq. (5), $x_t$ switches from the value $x_t = 1$ when $t = 0$ to $x_t = x < 1$ when $t > t_s$, the time of the shock. The initial condition is $\phi_s(t = 0) = \bar{\phi}_s$. We perform two sets of experiments for the dilution factors $x = 0.3$ and $x = 0.6$.

Such short timescale dynamics is used to estimate the non dimensional parameters $A$, $B$ and $\alpha$ and the timescale $\tau$. See Fig. 4. These values are close to those roughly estimated in Table 1 based on independent literature data, showing that the fitted values are realistic. This confirms that the simple model Eq. (3) is able to quantitatively capture some key features of cell volume regulation at a short timescale.

**Modification of the model in presence of GSDMD pores.** As we have already mentioned, a simplistic way to search for a steady state volume in the presence of GSDMD pores would be to consider a vanishingly small parameter $\alpha$ in Eq. (4) since GSDMD pores clearly permeabilize the PM to ions (Fig. 2 D). This however, necessarily leads to a vanishingly small $\bar{\phi}_s$ corresponding to an infinite swelling of the cell. Modulo a mechanical resistance of the cell membrane which is negligible, this would also happen with more refined models (23–27) which operate with a water flux that follows Eq. (1). This is because such description treats GSDMD pores in the same way as the selective ion channels, which is not correct since such pores are also permeable to water.

The problem can readily be realized by considering the pressure drop across a cylindrical hole in a membrane relating the flux of water per unit surface $j_w^p$ to the pressure variation $\Delta p$ in the following way :

$$j_w^p / \rho_w = \mathcal{R} \Delta p,$$

where $\mathcal{R}$ is the effective hydraulic resistance. See (37). The flux of ions per unit surface $s^p$ across the hole is

$$s^p = \rho_w \phi \mathcal{R} \Delta p,$$

where $\phi$ is the mass fraction of ions in the pore. We neglect the ion diffusive mobility in the pore based on the assumption that an electrochemical constraint controls the mass fraction of ions in the pore sufficiently fast. See (37) for a detailed model.

With the purely entropic free energy $f(\phi) = RT(\phi \ln \phi - \phi)/M$ describing the ions mixing with the solvent, the osmotic pressure reads $\Pi = \rho_w(\phi \partial_\phi f - f) = \rho_w RT\phi/M$ and the ions chemical potential is $\mu = \partial_\phi f = RT/M \ln \phi$. We thus obtain:

$$\begin{pmatrix} j_w^p/\rho_w \\ s^p \end{pmatrix} = \mathcal{R} \begin{bmatrix} 1 & \rho_w \phi \\ \rho_w \phi & (\rho_w \phi)^2 \end{bmatrix} \begin{pmatrix} \Delta p - \Delta\Pi \\ \Delta\mu \end{pmatrix},$$

showing the presence of cross-coefficients in the transport of water and ions through the PM in a non-selective case. To account for the presence of such coupling, we modify Eq. (2) in the following way (See (37) for the detailed derivation):

$$\begin{aligned} \tau \frac{d(\phi_s^{-1} - 1)}{dt} &= (1+n)(A\phi_s^2 + B\phi_s + \chi - 1) - \theta n \ln(\chi) \\ \tau \frac{d\chi(\phi_s^{-1} - 1)}{dt} &= \theta n (A\phi_s^2 + B\phi_s + \chi - 1) - (n\theta^2 + \epsilon) \ln(\chi) - \alpha\epsilon \end{aligned} \qquad [6]$$

The two additional non-dimensional parameters are $n$ representing the permeability to water due to the GSDMD pores in the PM compared to that due to the selective aquaporins and $\theta$ representing the filtration ratio of the GSDMD pores with respect to the ions.

Through both the selective channels and the GSDMD pores, an increase of the ion concentration in the cell will create an influx of water and cell swelling through direct osmosis to dilute the ions. However such increase will also create an efflux of ions to equilibrate the ion concentrations across the PM. See Fig. 6 (A). This ion flux will create a proportional efflux of water through the pores, decreasing the cell volume. The competition between these two phenomena will fix the steady state volume. The cross effect also happens symmetrically (21) at the level of ions which flux is no longer only proportional to their difference of concentrations across the PM, but also contains a contribution proportional to the water flux going through the pores and transporting ions. Both direct osmosis and cross-transport are proportional to the number of pores, so the full permeabilization of the PM by the GSDMD pores is not a trivial limit since both terms are still competing.

DRAFT

As a matter of fact, we find that Eq. (6) can still have a finite steady state generalizing Eq. (4) when the permeability to water in the pores is large compare to that of the aquaporins ($n \gg 1$):

$$\bar{\phi}_s = \frac{\sqrt{4A\left(1-\theta\tilde{\alpha}-e^{-\tilde{\alpha}}\right)+B^2}-B}{2A} \text{ and } \bar{\chi} = e^{-\tilde{\alpha}}. \quad [7]$$

where the effective pump-to-leak ratio reads $\tilde{\alpha} = \alpha\epsilon/(\theta^2+\epsilon)$. We recover the steady state expressions Eq. (4) when $\theta = 0$, which corresponds to a selectivity of the GSDMD pores since only water can get through in this degenerate case. Eq. (7) is only valid in the a range of $0 \leq \theta \leq \theta_m$ where $\theta_m$ satisfies:

$$\alpha\epsilon\theta_m\left(\theta_m^2+\epsilon\right) = 1 - e^{-\frac{\alpha\epsilon}{\theta_m^2+\epsilon}}.$$

In this range $\bar{\phi}_s$ remains finite and is given by Eq. (7) while if $\theta > \theta_m$, the cell swells to infinity.

Based on these theoretical results, our interpretation of the two phases swelling of the cell volume separated by a slow down/plateau is the following. The initial formation of GSDMD pores achieves a large permeabilization of the membrane with respect to water and ions. In the model, this can be related to $n$ increasing from zero (in the absence of GSDMD pores) to a large value, while $\theta$ representing the filtration of GSDMD pores with respect to ions, remains fixed at a value $\theta_0$ smaller than the critical value $\theta_m$ beyond which no finite swelling is accessible. The consequence is a first swelling phase from the initial homeostatic volume given by Eq. (4) to a shoulder/plateau-like value given by Eq. (7). However, there is still a slow evolution along that dynamics corresponding to the pores getting larger, which accelerates close to the end of the plateau. Such evolution can be captured in the model by a slow increase of $\theta$. When $\theta$ gets towards the critical value $\theta_m$, a second swelling phase occurs since no finite volume steady state is any longer accessible. Note that $\theta$ is an effective parameter in the model representing the level of filtration of the PM by non-selective pores with the radius of the pore clearly playing an important role in its ability to control its internal ions concentrations. Such pores are not only represented by GSDMD as Ninj1 also clearly brings a contribution. We show on Fig. 6 (B) how a realistic dynamic of the cell volume swelling can be captured within our simple model.

## Discussion

For long, the mechanisms leading to PM rupture and the release of large molecules during pyroptosis have remained elusive. Recent discoveries of key players, such as GSDMD and Ninj1, have shed light on the underlying molecular mechanisms, significantly enhancing our understanding of the process. Nevertheless, the physical basis of cell swelling and PM rupture remains unclear, as do the precise roles of these players and the chronological sequence of events. In a previous study, we demonstrated that pyroptotic swelling is a two-step process with uncharacterized sequential and molecular events (31). Here, we combined an improved FXm resolution with theoretical modeling and showed that the swelling dynamics can arise from a progressive permeation of the PM by non selective pores.

Indeed, we showed that cells start to swell as soon as the PM is permeable to small dyes and thus ions. However,

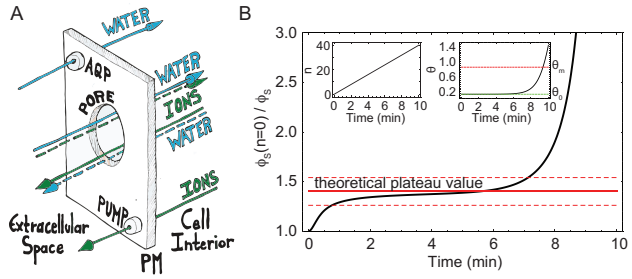


**Fig. 6.** (A) Schematic of modelling of the transport at the plasma membrane at the volume plateau when pores are non selective for water and ions with coupling between the two fluxes setting the steady state volume. (B) Swelling dynamics obtained with model Eq. (6) with the pore formation dynamics $n$ and the evolution of the pore filtration ratio $\theta$ both given in inserts. The first swelling phase is due to the dynamics of $n$ reaching a large value while the second swelling phase is due to the pores getting larger and subsequently becoming unable to control their inner ions concentration. Parameters are $\epsilon = 10^{-2}$, $A = 93$, $B = 3.7$, $\alpha = 1.9$ and $\tau = 1$s.

even though the PM permeability keeps increasing with the formation of GSDMD pores, this initial swelling slows down and we can even observe a volume plateau that lasts several minutes before another phase of swelling. The establishment of this plateau is puzzling and cannot be explained by models classically used to describe volume regulation in mammalian cells in which it is the active efflux of ions from pumps that can screen the passive osmotic swelling (23). In our conditions, as the permeability of the PM is large and the pumps cannot run at an irrealistic pace, such model would predict an infinite cell swelling.

To explain the origin of the volume plateau, we first established the foundation of our model in the absence of pyroptotic pores at the plasma membrane. Our model is a simple variant of classical pump and leak models (23–27, 43, 44). Our main difference with these models is that we do not consider for simplicity the well-known role of electostatics in osmosis, but we take into consideration a generic entropy of mixing between biopolymers in solution in the cytosol. Our model can then quantitatively capture the short timescale cell's passive response to osmotic perturbations with realistic parameters. This demonstrates that our model can be applied to quantify key membrane permeability properties, such as the water filtration coefficient and the ions pump to leak ratio (Fig. 5).

Then, we considered that the pores formed during pyroptosis are non selective and thus permeable to ions and water since small dyes can pass through. This introduces a coupling between the fluxes of water and ions at the membrane (See Eq. (6) and Fig. 6 A). The competition between water fluxes in the aquaporins and the pores and that of the ions in the pumps/channels and in the pores provides the possibility to obtain a volume plateau even in the presence a large PM permeability. The formation and the non-selectivity of the pores are captured by two parameters in the model, one accounting for the permeability introduced by the pores ($n$) and one for their finite selectivity with respect to ions ($\theta$). See Eq. (6). Our interpretation of the two-steps swelling is then the following: The first swelling phase is due to the full membrane permeabilization. This phase reaches a volume steady state when the PM permeability due to the pores is becoming much larger than that due to the

DRAFT

aquaporins. However, this only occurs in certain range of the pore selectivity. The fact that pores effectively become larger (first slowly and then more rapidly, see Fig. 3 (F)) suggests that the pores become less and less selective over time. As a result, the parameter $\theta$ is expected to increase beyond the critical threshold beyond which no steady state volume is anymore possible, as in classical pump and leak models. This is at the origin of the second swelling phase that culminates with the PM rupture.

Pyroptosis was long thought to result from the formation of a hypothetical 'death channel' that induced swelling and cell death (46). However, it is now established that GSDMD pore formation at the plasma membrane is a prerequisite for membrane lysis by Ninj1 ((37), (4, 16, 47)). GSDMD pores form within minutes, initially assembling as oligomeric arcs and slits that already permeabilize the membrane (7, 48). Our findings suggest that the first phase of swelling corresponds to the oligomerization and enlargement of GSDMD pores. However, the second swelling phase is likely driven by Ninj1 lesions, as dyes larger than the effective size of GSDMD pores can cross the plasma membrane. In addition, the observed increase in membrane permeability follows two distinct dynamics, supporting the involvement of two molecular players (Fig. 3 F). However, it remains unclear whether the end of the plateau - marking the onset of the second swelling phase - is triggered by further expansion of GSDMD pores or the opening of Ninj1 lesions. A compelling hypothesis suggests that Ninj1 lesion formation may be mechanically induced, specifically by an increase in plasma membrane tension (49, 50). In that frame, a complete opening of GSDMD pores is likely to trigger the second swelling phase and concomitantly Ninj1 membrane lesions via a PM tension increase.

Since most forms of programmed lytic cell death involve significant volume changes and tightly regulated membrane permeability, our approach, combining quantitative volume and permeability tracking with theoretical modeling, offers new insights into both the physical and molecular mechanisms at play. Moreover, comparing different cell death pathways - whether they share volume or permeability dynamics and molecular players or not - can shed light on the underlying physics governing these highly regulated yet dramatic events. For instance, using optogenetic activation, we explored a binary ON/OFF mechanism (31), yet other activators can trigger more graded response for various cell death (51). Capturing the dynamics of gradual activation and healing will definitely provide valuable insights on more subtle events.

## Materials and Methods

**Reagents.** Sulfo-Rhodamine B (SRB) was purchased from Sigma-Aldrich. Alexa-Fluor 647-Dextran 10 kDa was purchased from Thermo Fisher. TRITC-Dextran 4.4 kDa, FITC-Dextran 70 kDa, and TRITC-Dextran 500 kDa were purchased from Tdb Labs (Sweden). Polydimethylsiloxane (PDMS), Sylgard 184, was obtained from Dow Corning.

**Cell lines expressing optogenetic constructs for the selective activation of pyroptosis.** Murine immortalized bone marrow-derived macrophages (iBMDM) and mouse embryonic fibroblast (MEF) cell lines stably express an optogenetic construct composed of human ASC, CRY2, and TagRFP, named opto-ASC. This optogenetic tool has been shown to trigger inflammasome activation upon light stimulation and perfectly recapitulates classical pyroptosis activation involving cell swelling. (31) Fig.1 A). Briefly, upon light activation, CRY2 induces the polymerization of ASC which forms the inflammasome and activates caspase 1. Caspase 1 cleaves proinflammatory molecules and GSDMD, which subsequently translocates to the PM to form a GSDMD pore, inducing cell swelling and PM rupture. The optogenetic approach enables rapid and specific activation of the pathway without interference or background, as compared with drug-inducible systems that can impact PM permeability. The iBMDM cell line naturally expresses caspase-1, a central player in the pyroptosis process, whereas the MEF cell line was stably transduced to express caspase-1 (31). Cells were cultured in DMEM (Dulbecco's Modified Eagle Medium) with 4.5 g/L glucose (Gibco) supplemented with 10% FBS (fetal bovine serum), 1% penicillin-streptomycin, 1% Glutamax, and 1% sodium pyruvate (all from Invitrogen).

**Live imaging to correlate cell morphology and PM permeability during pyroptosis.** Pyroptosis process imaging were performed in a controlled atmosphere (37$^o$C, 5% CO2) with a spinning disk confocal microscope Yokogawa CSU-W1 (Objective 40x). Cells were seeded into ibidi µ-slides (VI 0.1), in phenol red-free medium 24 h before the experiment. The medium was then replaced by imaging medium supplemented with 1 g/l of 70 kDa conjugated to FITC. Optogenetic construct was activated with a 488 nm laser (three times every 10 seconds). Z-stack and timelapse (one image every 15 s) acquisitions were performed over 45 mins to concomitantly visualize speck formation (RFP), bleb appearance, and dextran entry through the PM. Bleb formation was visualized using brightfield microscopy, specks were imaged using a 561 nm laser, and dextran entry coupled to FITC was visualized 488 nm laser. Image analysis was performed with Fiji software.

**Fabrication of fluorescence exclusion microscopy chips.** Chips presenting a microfluidic chamber of defined height (20.3 µm) were made by pouring PDMS elastomer and curing agent (1:10, Sylgard 184 from Dow Corning) on a mold and were cured for at least 2 h at 65$^o$C. Molds were made on a silicon wafer with SU-8 photoresist using classical photolithography techniques. 3 mm inlets and outlets in the PDMS were punched, and the PDMS chips were cut to fit on glass coverslips. Chips were bonded to glass coverslips by exposure to air plasma for 30 s. The coverslips were bonded onto 35 petri dishes with Norland Optical Adhesive 81 (Norland) for 1 minute at UV 324 nm. These systems are UV 324 nm sterilized for 15 mins and could then be stored for a week in PBS at +4$^o$C prior to seeding cells.

**Cell Volume measurement with FXm.** Cell volumes were obtained using the fluorescence exclusion method (FXm) as detailed in (35, 52). Briefly, cells are seeded in a chamber with a height of 20 µm within microfluidic chips and incubated with non-permeable fluorescent dyes of increasing hydrodynamic diameter (Fig.1 B&C)). At cell location, fluorescence is excluded since the dye cannot enter the cell. Given that fluorescence intensity is known for the defined chamber height, cell volume is calculated by integrating the fluorescence intensity over the cell area. Cell swelling is assessed by monitoring the decrease in fluorescence intensity until the cells become permeable to the dyes, indicating PM permeability and the dynamics of PM pore opening.

The day before the experiment, PBS in the chip was replaced by culture medium, and the chips were incubated at 37$^o$C overnight to allow the PDMS to saturate with culture medium. Then, $5 \times 10^4$ cells were plated on the PDMS chip with phenol-free medium supplemented with HEPES one day before the experiments. For volume measurement, phenol red-free medium was supplemented with a fluorescent dye. Fluorescence was thus excluded by the cells, and cell volumes were obtained by integrating the fluorescence intensity over the cell.

To precisely monitor variations in cell volume and plasma membrane (PM) permeability until PM rupture during pyroptosis, we used fluorescent dyes with increasing hydrodynamic radii: SRB ($\simeq$ 0.5 nm), 4.4 kDa Dextran-TRITC ($\simeq$ 1 nm), 10 kDa Dextran-Alexa Fluor 637 ($\simeq$ 1.9 nm), 70 kDa Dextran-FITC ($\simeq$ 6.5 nm), and 500 kDa Dextran-TRITC ($\simeq$ 15.9 nm) (Fig. 1 B). In the first set of experiments, we characterized changes in cell volume and PM permeability during pyroptosis. SRB and 10 kDa Dextran-

DRAFT

Alexa Fluor 637 were co-incubated to detect the initial loss of PM integrity, with SRB serving as an early permeability marker. Global cell volume variations were monitored using the concurrent incubation of 10 kDa Dextran-Alexa Fluor 637 and 500 kDa Dextran-TRITC. Due to their respective hydrodynamic radii, 10 kDa Dextran-Alexa Fluor 637 enters cells through GSDMD pores ($\simeq$ 10.75 nm radius), whereas 500 kDa Dextran-TRITC enters only after PM rupture. The second set of experiments aimed to assess the full range of PM permeability changes during pyroptosis. Cells were incubated with either 4.4 kDa Dextran-TRITC, 10 kDa Dextran-Alexa Fluor 637, and 70 kDa Dextran-FITC, or with 10 kDa Dextran-Alexa Fluor 637, 70 kDa Dextran-FITC, and 500 kDa Dextran-TRITC. The inclusion of 10 kDa Dextran-Alexa Fluor 637 in all conditions ensured consistency across experiments, allowing for accurate comparison of PM permeability changes throughout pyroptosis.

Acquisitions were performed at 37$^o$C using an epifluorescence microscope (Leica DMi8) with a 10x objective (NA. 0.3, LEICA). Light activation of pyroptosis through optogenetic construction was performed with a 488 nm LED (25% of a PE300 LED from CoolLED) for 10 seconds, delivering a light dose of 3720 mJ/cm$^2$. Cell volume was then monitored with a 8-second frame rate using 488 nm, 560 nm, and 635 nm LEDs to visualize FITC, TRITC or SRB, and Alexa Fluor 647 fluorescence, respectively, from the dye pack described above.

For osmtic shocks, dedicated FXm chambers with low flow resistance were used to reduce the time for medium injection below 1 second (26) . The surface of the microfluidic chambers was coated right after plasma bonding with 0.01% poly-L-lysine solution for 30 minutes (Sigma-Aldrich). Cells were injected and allowed to adhere for 15 minutes before injection of the fluorophore-containing medium (Alexa-647 10 kDa dextran). Cell volume monitoring using FxM was initiated under isotonic conditions, after which the medium was exchanged for a known hypotonic solution supplemented with a similar concentration of fluorescent dye. The whole process was performed during continuous FXm acquisition with a 100 ms frame rate using 635 nm LEDS to visualize Alexa Fluor 647 fluorescence. The hypoosmotic solution was prepared by adding water to the culture medium.

**Image analysis: Cell volume and PM permeability extraction.** Image analysis was performed using a homemade MATLAB program adapted from (35, 36). Briefly, for every time frame, the fluorescence background is subtracted for each cell, and the linear relation between fluorescence and known chamber height is calibrated for each field in view. For multiple dyes, cell segmentation is systematically performed on the images of the largest dye since it is the last to enter the cells. The fluorescence drop is integrated over the area of each cell obtained from the segmentation and computed in volume using the relation between fluorescence and height obtained previously. The time points of interest were manually extracted from the cell volume kinetic curve obtained at the single-cell level for each dye.

The FxM signal obtained with SRB is used to determine the initial loss of PM permeability, marked by a decrease in the signal cell volume.

Concerning Dextran dyes, $T_0$ marks the start of cell swelling, characterized by an increase in cell volume. $T_1$ is the end of the cell swelling phase, as measured with the observed fluorescent dye. $T_2$ corresponds to the fluorescent dye entry in the cell, indicating a loss of plasma membrane (PM) permeability relative to the observed dye size. For each dextran, the $\Delta T$ between SRB entry and $T_2$ was calculated to determine their sequential entry into the cell. After $T_2$, fluorescence increases in cell, and cell volume is not longueur assessed until the end of the experiment (40 minutes after optogenetic activation). At each time point, corresponding cell volume values $V_0$, $V_1$ and $V_2$ are determined.

The FxM signal obtained with 500 kDa-Dextran-TRITC, which has the largest hydrodynamic diameter, was used to track all cell volume changes during the pyroptosis process. This dye was also used to detect the global cell swelling phase between $T_0$ and $T_1$, as well as to identify the timing of PM rupture ($T_2$) and corresponding cell volume ($V_2$).

Cell volume plateau characteristics were determined from the FxM signal obtained with 10 kDa-Dextran-AlexaFluor 647, when all Dextran signals followed the same trend. The occurrence of the cell volume plateau is identified when the cell volume stabilizes during the swelling phase, which is defined, as previously described with 500 kDa-Dextran-TRITC, by the condition $(V_2 - V_1)/V_0 < 10\%$ , and its duration $T_2 - T_1$ exceeds 1 minute. $\Delta V_p/V_i$ is then calculated based on $V_1/V_0$ obtained previously. Each experiment was performed at least three times independently.

**Fitting parameters for osmotic shocks.** For iBMDM cells, we find the fitting parameters $A = 92.50 \pm 1.23$, $B = 4.40 \pm 0.65$, $\alpha = 2.07 \pm 0.36$ and $\tau = 1.09 \pm 0.28$ s for $x = 0.6$ and $A = 93.35 \pm 1.35$, $B = 3.79 \pm 0.63$, $\alpha = 2.26 \pm 0.35$ and $\tau = 0.99 \pm 0.26$s for $x = 0.3$.

For MEF cells, we find the fitting parameters $A = 75.73 \pm 23.55$, $B = 7.50 \pm 4.27$, $\alpha = 5.18 \pm 1.82$ and $\tau = 0.43 \pm 0.32$ s for $x = 0.6$ and $A = 88.22 \pm 13.34$, $B = 3.97 \pm 3.83$, $\alpha = 6.76 \pm 2.02$ and $\tau = 0.56 \pm 0.50$s for $x = 0.3$.

**Statistical analysis.** Statistical analyses were performed using MATLAB. Two-tailed paired Student t-test was used, and significance was accepted at the 96 % confidence level (** $p < 0.05$).

**Author contributions.** Conceptualization: E.B, S.M. and P.R.; methodology: E.B., S.M.and P.R; investigation: E.B, G.D. and H.D; writing – original draft: E.B, S.M. and P.R.; draft editing: E.B, S.M., P.R., H.D, C.R., V.P.; resources: V.P.; funding acquisition: S.M., P.R.,V.P. and C.R.; Supervision: E.B, S.M. and P.R.

**Competing interest.** The authors declare no competing interest

**ACKNOWLEDGMENTS.** We thank Matthieu Mercury from ILM for the drawings illustrating the article. Funding: This work was supported by the project SurVol PRC ANR-19-CE13-0030 (to E.B and P.R), Institut Convergence PLAsCAN, ANR-17-CONV-0002 (to E.B., V.P. and S.M.); PRC ANR-19-CE13-0030 (to E.B.and P.R.). ETOILE 2022 funding (to E.B. and C.R); CLARA cancéropole (to V.P.); Ligue Nationale Contre le Cancer comité de l'Ain (to V.P.); ANR-22-ce15-0032-01 (to V.P).

1. SB Kovacs, EA Miao, Gasdermins: Effectors of Pyroptosis. *Trends Cell Biol.* **27**, 673–684 (2017) Publisher: Elsevier Ltd.
2. K Schroder, J Tschopp, The Inflammasomes. *Cell* **140**, 821–832 (2010) Publisher: Elsevier.
3. J Shi, et al., Cleavage of GSDMD by inflammatory caspases determines pyroptotic cell death. *Nature* **526**, 660–665 (2015).
4. X Liu, et al., Inflammasome-activated gasdermin D causes pyroptosis by forming membrane pores. *Nature* **535**, 153–158 (2016) Publisher: Nature Publishing Group.
5. S Rühl, P Broz, Regulation of Lytic and Non-Lytic Functions of Gasdermin Pores. *J. Mol. Biol.* **434** (2022).
6. SL Fink, BT Cookson, Caspase-1-dependent pore formation during pyroptosis leads to osmotic lysis of infected host macrophages. *J. Immunol.* **202**, 1913–1926 (2006).
7. L Sborgi, et al., GSDMD membrane pore formation constitutes the mechanism of pyroptotic cell death. *The EMBO J.* **35**, 1766–1778 (2016).
8. SL Schaefer, G Hummer, Sublytic gasdermin-D pores captured in atomistic molecular simulations. *eLife* **11**, e81432 (2022) Publisher: eLife Sciences Publications, Ltd.
9. E Mulvihill, et al., Mechanism of membrane pore formation by human gasdermin-d. *The EMBO journal* **37**, e98321 (2018).
10. AB Santa Cruz Garcia, KP Schnur, AB Malik, GCH Mo, Gasdermin D pores are dynamically regulated by local phosphoinositide circuitry. *Nat. Commun.* **13**, 52 (2022) Number: 1 Publisher: Nature Publishing Group.
11. X Chen, et al., Pyroptosis is driven by non-selective gasdermin-D pore and its morphology is different from MLKL channel-mediated necroptosis. *Cell Res.* **26**, 1007–1020 (2016) Publisher: Nature Publishing Group.
12. L DiPeso, DX Ji, RE Vance, JV Price, Cell death and cell lysis are separable events during pyroptosis. *Cell Death Discov.* **3**, 1–10 (2017) Publisher: The Author(s).
13. R Heilig, et al., The gasdermin-d pore acts as a conduit for il-1$\beta$ secretion in mice. *Eur. journal immunology* **48**, 584–592 (2018).
14. CL Evavold, et al., The pore-forming protein gasdermin d regulates interleukin-1 secretion from living macrophages. *Immunity* **48**, 35–44 (2018).
15. J Van Oostrum, JP Priestle, MG Grutter, A Schmitz, The structure of murine interleukin-1 $\beta$ at 2.8 a resolution. *J. structural biology* **107**, 189–195 (1991).
16. N Kayagaki, et al., NINJ1 mediates plasma membrane rupture during lytic cell death. *Nature* (2021).
17. S Kappelhoff, EG Margheritis, K Cosentino, New insights into Gasdermin D pore formation. *Biochem. Soc. Transactions* **52**, 681–692 (2024).
18. B Hille, Ionic channels in excitable membranes. current problems and biophysical approaches. *Biophys. journal* **22**, 283–294 (1978).
19. L David, et al., NINJ1 mediates plasma membrane rupture by cutting and releasing membrane disks. *Cell* **187**, 2224–2235.e16 (2024).
20. P Devant, JC Kagan, Molecular mechanisms of gasdermin D pore-forming activity. *Nat. Immunol.* **24**, 1064–1075 (2023) Publisher: Nature Publishing Group.

DRAFT

21. O Kedem, A Katchalsky, Thermodynamic analysis of the permeability of biological membranes to non-electrolytes. *Biochimica et biophysica Acta* **27**, 229–246 (1958).
22. C Cadart, L Venkova, P Recho, MC Lagomarsino, M Piel, The physics of cell-size regulation across timescales. *Nat. Phys.* **15**, 993–1004 (2019).
23. J Keener, J Sneyd, *Mathematical physiology 1: Cellular physiology*. (Springer New York, NY, USA), (2009).
24. H Jiang, SX Sun, Cellular pressure and volume regulation and implications for cell mechanics. *Biophys. journal* **105**, 609–619 (2013).
25. RM Adar, SA Safran, Active volume regulation in adhered cells. *Proc. Natl. Acad. Sci.* **117**, 5604–5609 (2020).
26. L Venkova, et al., A mechano-osmotic feedback couples cell volume to the rate of cell deformation. *Elife* **11**, e72381 (2022).
27. R Rollin, JF Joanny, P Sens, Physical basis of the cell size scaling laws. *Elife* **12**, e82490 (2023).
28. B Alberts, et al., *Molecular Biology of the Cell*. p. 661 (2022).
29. F Sachs, MV Sivaselvan, Cell volume control in three dimensions: Water movement without solute movement. *J. Gen. Physiol.* **145**, 373–380 (2015).
30. C Roffay, et al., Passive coupling of membrane tension and cell volume during active response of cells to osmosis. *Proc. Natl. Acad. Sci.* **118**, e2103228118 (2021).
31. J Nadjar, et al., Optogenetically controlled inflammasome activation demonstrates two phases of cell swelling during pyroptosis. *Sci. Signal.* **17**, eabn8003 (2024) Publisher: American Association for the Advancement of Science.
32. S Ramos, E Hartenian, P Broz, Programmed cell death: NINJ1 and mechanisms of plasma membrane rupture. *Trends Biochem. Sci.* **49**, 717–728 (2024) Publisher: Elsevier.
33. KA Granath, BE Kvist, Molecular weight distribution analysis by gel chromatography on sephadex. *J. Chromatogr. A* **28**, 69–81 (1967).
34. Physical properties of dextran molecules and fractions (https://dextran.com/dextran-chemistry/physical-properties-dextran/dextran.com).
35. E Zlotek-Zlotkiewicz, S Monnier, G Cappello, M Le Berre, M Piel, Optical volume and mass measurements show that mammalian cells swell during mitosis. *The J. cell biology* **211**, 765 (2015).
36. C Cadart, et al., Size control in mammalian cells involves modulation of both growth rate and cell cycle duration. *bioRxiv* p. 152728 (2017) arXiv: 152728 Publisher: Springer US ISBN: 4146701805.
37. See supplementary information (https://) (2025).
38. PJ Flory, Thermodynamics of high polymer solutions. *The J. chemical physics* **10**, 51–61 (1942).
39. B Hille, *Ionic Channels of Excitable Membranes*. (Oxford University Press, Incorporated), (1992).
40. T Clausen, Quantification of na+, k+ pumps and their transport rate in skeletal muscle: functional significance. *J. Gen. Physiol.* **142**, 327–345 (2013).
41. L Nordahl, et al., Detection and quantification of na, k-atpase dimers in the plasma membrane of living cells by fret-fcs. *Biochimica et Biophys. Acta (BBA)-General Subj.* **1868**, 130619 (2024).
42. H Elmoazzen, J Elliott, L McGann, The effect of temperature on membrane hydraulic conductivity. *Cryobiology* **45**, 68–79 (2002).
43. Y Mori, Mathematical properties of pump-leak models of cell volume control and electrolyte balance. *J. mathematical biology* **65**, 875–918 (2012).
44. AR Kay, How cells can control their size by pumping ions. *Front. cell developmental biology* **5**, 41 (2017).
45. H Lodish, *Molecular Cell Biology*, Cd-Rom. (W.H. Freeman), (2000).
46. Y Nishimura, JJ Lemasters, Glycine blocks opening of a death channel in cultured hepatic sinusoidal endothelial cells during chemical hypoxia. *Cell Death Differ.* **8**, 850–858 (2001).
47. Wt He, et al., Gasdermin d is an executor of pyroptosis and required for interleukin-1$\beta$ secretion. *Cell Res.* **25**, 1285–1298 (2015) Publisher: Nature Publishing Group.
48. S Kappelhoff, et al., Structure and regulation of GSDMD pores at the plasma membrane of pyroptotic cells (2023) Pages: 2023.10.24.563742 Section: New Results.
49. E Hartenian, et al., Ninjurin-1 mediated plasma membrane rupture is a two-step process requiring cell swelling (2024) Pages: 2024.10.29.620849 Section: New Results.
50. J Xu, et al., NINJ1 regulates plasma membrane fragility under mechanical tension (2024) ISSN: 2693-5015.
51. K Shkarina, et al., Optogenetic activators of apoptosis, necroptosis, and pyroptosis. *J. Cell Biol.* **221** (2022).
52. C Cadart, et al., Fluorescence exclusion measurement of volume in live cells in *Methods in cell biology*. (Elsevier) Vol. 139, pp. 103–120 (2017).


DRAFT